Damage morphology for picosecond pulses at 1053 nm for silica optics

T. A. Laurence, S. Ly, N. Shen, W. Carr, D. Alessi, J. Bude, A. Rigatti

July 13, 2016

Disclaimer

This document was prepared as an account of work sponsored by an agency of the United States government. Neither the United States government nor Lawrence Livermore National Security, LLC, nor any of their employees makes any warranty, expressed or implied, or assumes any legal liability or responsibility for the accuracy, completeness, or usefulness of any information, apparatus, product, or process disclosed, or represents that its use would not infringe privately owned rights. Reference herein to any specific commercial product, process, or service by trade name, trademark, manufacturer, or otherwise does not necessarily constitute or imply its endorsement, recommendation, or favoring by the United States government or Lawrence Livermore National Security, LLC. The views and opinions of authors expressed herein do not necessarily state or reflect those of the United States government or Lawrence Livermore National Security, LLC, and shall not be used for advertising or product endorsement purposes.

The Role of Defects in Laser-induced Modifications of Silica Coatings and Fused Silica Using Picosecond Pulses at 1053 nm: I. Damage Morphology

S. LY,[1] N. SHEN,[1] R. A. NEGRES,[1] C. W. CARR,[1] D. A. ALESSI,[1] J. D. BUDE,[1] A. RIGATTI,[2] AND T. A. LAURENCE[1,*]

[1]NIF and Photon Sciences, Lawrence Livermore National Laboratory, 7000 East Avenue, Livermore, CA, 94550

[2]Laboratory for Laser Energetics, University of Rochester, Rochester, NY
*laurence2@llnl.gov

Abstract: Laser-induced damage with ps pulse widths straddles the transition from intrinsic, multi-photon ionization and avalanche ionization-based ablation with fs pulses to defect-dominated, thermal-based damage with ns pulses. We investigated the morphology of damage for fused silica and silica coatings between 1 ps and 60 ps at 1053 nm. Using calibrated laser-induced damage experiments, *in situ* imaging, and high-resolution optical microscopy, atomic force microscopy, and scanning electron microscopy, we show that defects play an important role in laser-induced damage down to 1 ps. Three types of damage are observed: ablation craters, ultra-high density pits, and smooth, circular depressions with central pits. For 10 ps and longer, the smooth, circular depressions limit the damage performance of fused silica and silica coatings. The observed high-density pits and material removal down to 3 ps indicate that variations in surface properties limit the laser-induced damage onset to a greater extent than expected below 60 ps. Below 3 ps, damage craters are smoother although there is still evidence as seen by AFM of inhomogeneous laser-induced damage response very near the damage onset. These results show that modeling the damage onset only as a function of pulse width does not capture the convoluted processes leading to laser induced damage with ps pulses. It is necessary to account for the effects of defects on the processes leading to laser-induced damage. The effects of isolated defects or inhomogeneities are most pronounced above 3 ps but are still discernible and possibly important down to the shortest pulse width investigated here.

References

1. W. Rudolph, L. Emmert, Z. Sun, D. Patel, and C. Menoni, "Laser damage in dielectric films: What we know and what we don't," in G. J. Exarhos, V. E. Gruzdev, J. A. Menapace, D. Ristau, and M. Soileau, eds. (2013), p. 888516.
2. L. Gallais, B. Mangote, M. Zerrad, M. Commandré, A. Melninkaitis, J. Mirauskas, M. Jeskevic, and V. Sirutkaitis, "Laser-induced damage of hafnia coatings as a function of pulse duration in the femtosecond to nanosecond range," Appl. Opt. **50**, C178–C187 (2011).
3. P. E. Miller, J. D. Bude, T. I. Suratwala, N. Shen, T. A. Laurence, W. A. Steele, J. Menapace, M. D. Feit, and L. L. Wong, "Fracture-induced subbandgap absorption as a precursor to optical damage on fused silica surfaces," Opt. Lett. **35**, 2702–2704 (2010).
4. C. Carr, J. Bude, and P. DeMange, "Laser-supported solid-state absorption fronts in silica," Phys. Rev. B **82**, 184304 (2010).

5. S. G. Demos, R. A. Negres, R. N. Raman, A. M. Rubenchik, and M. D. Feit, "Material response during nanosecond laser induced breakdown inside of the exit surface of fused silica: Material response during nanosecond laser," Laser Photonics Rev. **7**, 444–452 (2013).

6. L. Gallais, J. Capoulade, J.-Y. Natoli, and M. Commandré, "Investigation of nanodefect properties in optical coatings by coupling measured and simulated laser damage statistics," J. Appl. Phys. **104**, 053120 (2008).

7. S. Papernov and A. W. Schmid, "Two mechanisms of crater formation in ultraviolet-pulsed-laser irradiated SiO2 thin films with artificial defects," J. Appl. Phys. **97**, 114906 (2005).

8. H. Wang, H. Qi, B. Wang, Y. Cui, M. Guo, J. Zhao, Y. Jin, and J. Shao, "Defect analysis of UV high-reflective coatings used in the high power laser system," Opt. Express **23**, 5213–5220 (2015).

9. T. A. Laurence, J. D. Bude, N. Shen, T. Feldman, P. E. Miller, W. A. Steele, and T. Suratwala, "Metallic-like photoluminescence and absorption in fused silica surface flaws," Appl. Phys. Lett. **94**, 151114 (2009).

10. P. E. Miller, J. D. Bude, T. I. Suratwala, N. Shen, T. A. Laurence, W. A. Steele, J. Menapace, M. D. Feit, and L. L. Wong, "Fracture-induced subbandgap absorption as a precursor to optical damage on fused silica surfaces," Opt. Lett. **35**, 2702–2704 (2010).

11. C. Carr, J. Bude, and P. DeMange, "Laser-supported solid-state absorption fronts in silica," Phys. Rev. B **82**, 184304 (2010).

12. S. G. Demos, R. A. Negres, R. N. Raman, A. M. Rubenchik, and M. D. Feit, "Material response during nanosecond laser induced breakdown inside of the exit surface of fused silica: Material response during nanosecond laser," Laser Photonics Rev. **7**, 444–452 (2013).

13. B. Chimier, O. Uteza, N. Sanner, M. Sentis, T. Itina, P. Lassonde, F. Legare, F. Vidal, and J. C. Kieffer, "Damage and ablation thresholds of fused-silica in femtosecond regime," Phys. Rev. B **84**, (2011).

14. L. Gallais and M. Commandré, "Laser-induced damage thresholds of bulk and coating optical materials at 1030 nm, 500 fs," Appl. Opt. **53**, A186 (2014).

15. I. H. Chowdhury, A. Q. Wu, X. Xu, and A. M. Weiner, "Ultra-fast laser absorption and ablation dynamics in wide-band-gap dielectrics," Appl. Phys. A **81**, 1627–1632 (2005).

16. R. A. Mitchell, D. W. Schumacher, and E. A. Chowdhury, "Modeling crater formation in femtosecond-pulse laser damage from basic principles," Opt. Lett. **40**, 2189 (2015).

17. D. Nieto, J. Arines, G. M. O'connor, and M. T. Flores-Arias, "Single-pulse laser ablation threshold of borosilicate, fused silica, sapphire, and soda-lime glass for pulse widths of 500 fs, 10 ps, 20 ns," Appl. Opt. **54**, 8596 (2015).

18. B. C. Stuart, S. M. Herman, and M. D. Perry, "Laser-induced damage in dielectrics with nanosecond to subpicosecond pulses I: experimental," in *Laser-Induced Damage in Optical Materials: 1994* (1995), pp. 568–578.

19. L. Gallais, B. Mangote, M. Zerrad, M. Commandré, A. Melninkaitis, J. Mirauskas, M. Jeskevic, and V. Sirutkaitis, "Laser-induced damage of hafnia coatings as a function of pulse duration in the femtosecond to nanosecond range," Appl. Opt. **50**, C178–C187 (2011).

20. B. C. Stuart, M. D. Feit, S. Herman, A. M. Rubenchik, B. W. Shore, and M. D. Perry, "Nanosecond-to-femtosecond laser-induced breakdown in dielectrics," Phys. Rev. B **53**, 1749 (1996).

21. A. V. Smith and B. T. Do, "Bulk and surface laser damage of silica by picosecond and nanosecond pulses at 1064 nm," Appl Opt **47**, 4812–4832 (2008).

22. C. W. Carr, M. D. Feit, M. A. Johnson, and A. M. Rubenchik, "Complex morphology of laser-induced bulk damage in K[sub 2]H[sub (2−x)]D[sub x]PO[sub 4] crystals," Appl. Phys. Lett. **89**, 131901 (2006).

23. C. W. Carr, D. A. Cross, M. A. Norton, and R. A. Negres, "The effect of laser pulse shape and duration on the size at which damage sites initiate and the implications to subsequent repair," Opt Express **19**, A859–A864 (2011).

24. Z. Wu, H. Jiang, Z. Zhang, Q. Sun, H. Yang, and Q. Gong, "Morphological investigation at the front and rear surfaces of fused silica processed with femtosecond laser pulses in air," Opt. Express **10**, 1244–1249 (2002).

25. S. Chen, Y. Zhao, Z. Yu, Z. Fang, D. Li, H. He, and J. Shao, "Femtosecond laser-induced damage of HfO₂/SiO₂ mirror with different stack structure," Appl. Opt. **51**, 6188–6195 (2012).

26. E. S. Fulkerson, S. Telford, R. Deri, A. Bayramian, R. Lanning, E. Koh, K. Charron, and C. Haefner, "Pulsed power system for the HAPLS Diode Pumped Laser System," in *2015 IEEE Pulsed Power Conference (PPC)* (2015), pp. 1–6.

27. J. A. Albelo, P. Y. Pirogovsky, J. N. O'Brien, and B. W. Baird, "Picosecond laser micromachining of advanced semiconductor logic devices," in W. A. Clarkson, N. Hodgson, and R. K. Shori, eds. (2008), p. 687122.

28. C. Xu and F. W. Wise, "Recent Advances in Fiber Lasers for Nonlinear Microscopy," Nat. Photonics **7**, (2013).

29. H. C. H. Mulvad, L. K. Oxenlowe, M. Galili, A. T. Clausen, L. Gruner-Nielsen, and P. Jeppesen, "1.28 TBIT/s single-polarisation serial OOK optical data generation and demultiplexing," Electron. Lett. **45**, 280–281 (2009).

30. J. M. Di Nicola, S. T. Yang, C. D. Boley, J. K. Crane, J. E. Heebner, T. M. Spinka, P. Arnold, C. P. J. Barty, M. W. Bowers, T. S. Budge, K. Christensen, J. W. Dawson, G. Erbert, E. Feigenbaum, G. Guss, C. Haefner, M. R. Hermann, D. Homoelle, J. A. Jarboe, J. K. Lawson, R. Lowe-Webb, K. McCandless, B. McHale, L. J. Pelz, P. P. Pham, M. A. Prantil, M. L. Rehak, M. A. Rever, M. C. Rushford, R. A. Sacks, M. Shaw, D. Smauley, L. K. Smith, R. Speck, G. Tietbohl, P. J. Wegner, and C. Widmayer, "The commissioning of the

advanced radiographic capability laser system: experimental and modeling results at the main laser output," in A. A. S. Awwal and M. A. Lane, eds. (2015), p. 93450I.

31. A. Couairon and A. Mysyrowicz, "Femtosecond filamentation in transparent media," Phys. Rep. **441**, 47–189 (2007).

32. R. A. Negres, C. W. Carr, T. A. Laurence, K. Stanion, G. Guss, D. A. Cross, P. J. Wegner, and C. J. Stolz, "Laser-induced damage of intrinsic and extrinsic defects by picosecond pulses on multilayer dielectric coatings for petawatt-class lasers," Opt. Eng. **56**, 011008–011008 (2016).

33. T. A. Laurence, R. A. Negres, S. Ly, N. Shen, C. W. Carr, D. A. Alessi, A. Rigatti, and J. D. Bude, "The Role of Defects in Laser-induced Modifications of Silica Coatings and Fused Silica Using Picosecond Pulses at 1053 nm: II. Scaling Laws and the Density of Precursors," Submitted (2017).

34. T. I. Suratwala, P. E. Miller, J. D. Bude, W. A. Steele, N. Shen, M. V. Monticelli, M. D. Feit, T. A. Laurence, M. A. Norton, C. W. Carr, and L. L. Wong, "HF-Based Etching Processes for Improving Laser Damage Resistance of Fused Silica Optical Surfaces," J. Am. Ceram. Soc. **94**, 416–428 (2011).

35. J. Bude, P. Miller, S. Baxamusa, N. Shen, T. Laurence, W. Steele, T. Suratwala, L. Wong, W. Carr, D. Cross, and M. Monticelli, "High fluence laser damage precursors and their mitigation in fused silica," Opt. Express **22**, 5839 (2014).

36. R. A. Negres, I. Bass, K. A. Stanion, G. Guss, D. A. Cross, D. A. Alessi, C. Stolz, and C. W. Carr, "Apparatus and techniques for measuring laser damage resistance of large-area, multilayer dielectric mirrors for use with high energy, picosecond lasers," in *CLEO: Science and Innovations* (Optical Society of America, 2015), p. SM3M–5.

37. D. A. Alessi, C. W. Carr, R. P. Hackel, R. A. Negres, K. Stanion, J. E. Fair, D. A. Cross, J. Nissen, R. Luthi, G. Guss, J. A. Britten, W. H. Gourdin, and C. Haefner, "Picosecond laser damage performance assessment of multilayer dielectric gratings in vacuum," Opt. Express **23**, 15532 (2015).

38. I. Jovanovic, C. Brown, B. Wattellier, N. Nielsen, W. Molander, B. Stuart, D. Pennington, and C. P. J. Barty, "Precision short-pulse damage test station utilizing optical parametric chirped-pulse amplification," Rev. Sci. Instrum. **75**, 5193 (2004).

39. I. Jovanovic, C. G. Brown, C. A. Ebbers, C. P. J. Barty, N. Forget, and C. L. Blanc, "Generation of high-contrast millijoule pulses by optical parametric chirped-pulse amplification in periodically poled KTiOPO4," Opt Lett **30**, 1036–1038 (2005).

40. R. Trebino, K. W. DeLong, D. N. Fittinghoff, J. N. Sweetser, M. A. Krumbügel, B. A. Richman, and D. J. Kane, "Measuring ultrashort laser pulses in the time-frequency domain using frequency-resolved optical gating," Rev. Sci. Instrum. **68**, 3277–3295 (1997).

41. "ISO 21254-1:2011(en), Lasers and laser-related equipment — Test methods for laser-induced damage threshold — Part 1: Definitions and general principles," https://www.iso.org/obp/ui/#iso:std:iso:21254:-1:ed-1:v1:en.

42. T. A. Laurence, J. D. Bude, N. Shen, W. A. Steele, and S. Ly, "Quasi-continuum photoluminescence: Unusual broad spectral and temporal characteristics found in defective surfaces of silica and other materials," J. Appl. Phys. **115**, 083501 (2014).

43. M. Mero, B. Clapp, J. C. Jasapara, W. Rudolph, D. Ristau, K. Starke, S. Martin, and W. Kautek, "On the damage behavior of dielectric films when illuminated with multiple femtosecond laser pulses," Opt. Eng. **44**, 051107–051107 (2005).

44. M. Mero, J. Liu, W. Rudolph, D. Ristau, and K. Starke, "Scaling laws of femtosecond laser pulse induced breakdown in oxide films," Phys. Rev. B **71**, (2005).

45. Y. Xu, L. A. Emmert, and W. Rudolph, "Spatio-TEmporally REsolved Optical Laser Induced Damage (STEREO LID) technique for material characterization," Opt. Express **23**, 21607 (2015).

46. Y. Xu, L. A. Emmert, and W. Rudolph, "Determination of defect densities from spatiotemporally resolved optical-laser induced damage measurements," Appl. Opt. **54**, 6813–6819 (2015).

47. L. Gallais, D.-B. Douti, M. Commandré, G. Batavičiūtė, E. Pupka, M. Ščiuka, L. Smalakys, V. Sirutkaitis, and A. Melninkaitis, "Wavelength dependence of femtosecond laser-induced damage threshold of optical materials," J. Appl. Phys. **117**, 223103 (2015).

48. H. Wang, H. Qi, J. Zhao, B. Wang, and J. Shao, "Transition from isolated submicrometer pits to integral ablation of HfO2 and SiO2 films under subpicosecond irradiation," Opt. Commun. **387**, 214–222 (2017).

49. A. Mouskeftaras, "Study of the physical mechanisms involved in the femtosecond laser optical breakdown of dielectric materials," Theses, Ecole Polytechnique X (2013).

1. Introduction

Laser-induced damage of optical materials is a particularly interesting example of a laser-material interaction, in which the material itself is destroyed. Laser-induced damage for nanosecond (ns) pulses have been studied extensively [1–8]. Thermal processes due to native or extrinsic defects in the material dominate laser-induced damage in the ns-scale regime. For long, ns laser pulses, damage has been attributed to a variable density of isolated surface

defects (damage precursors) that absorb sub-band-gap light [9,10]. When a damage precursor gets hot enough, temperature-activated absorption in the bulk leads to the generation of a destructive absorption front followed by material ejection and fracture [11,12]. The typical morphology for exit surface, nanosecond damage sites is large, very rough, micron-deep pits with extensive lateral/radial fractures. These large sites obliterate much of the information about the initial precursor. In contrast, for much shorter femtosecond (fs) pulses [13–16], laser damage is primarily driven by multiphoton and avalanche ionization.

Even with the extensive studies in the ns and fs pulse regimes, the damage morphology with ps pulse widths has not been thoroughly explored [17–21]. The latter regime is important since there is a transition between the highly fractured damage sites [22,23] obtained at ns pulse widths and the smoother ablation pits obtained for sub-ps pulse widths [24,25]. Because the shape and structure of resulting damage sites provide clues behind the damage mechanisms, morphological studies in ps pulse regime are likely to elucidate the underlying physical processes governing the transition. Due to the ongoing effort in developing picosecond petawatt lasers [26], there is an increasing need to understand the damage mechanisms in bulk optics and in dielectric coatings. However, the uncertainty in the physics driving the breakdown by pulses in the ps-regime greatly complicates current efforts to model and improve performance limits and lifetimes of optics used in these laser systems. These optics consist of polarizers, bulk dielectrics, reflective coatings, and diffraction gratings, and have a wide range of scientific and industrial applications. Picosecond and sub-ps lasers are currently used in micromachining for industrial applications [27], nonlinear microscopy [28], optical communications [29], and laser fusion research [30]. For short pulse lengths, multi-layer dielectric coatings are used to create reflective optics that avoid detrimental nonlinear beam propagation effects through bulk optical materials [31]. Commonly used materials include silica and hafnia deposited layers. For example, advanced short pulse laser systems are typically limited in their final optics to <0.5 TW/cm^2 in the ps regime, making these systems inherently inefficient as well as large and costly. Knowledge gained from studying the damage mechanism in single layer coatings here can inform development of more complicated multilayer dielectric coatings. Alternating layers of the low index material (silica) and the high index material (hafnia), are typically used to create highly reflective mirrors with higher damage resistance [32].

To explore the morphology of the damage sites, we performed damage testing at 1053 nm with laser pulse widths ranging from 1 ps to 60 ps. Damage tests are performed using the 1/1 damage test procedure where each site is exposed to one laser shot. Many sites are shot with varying energies of the laser beam. The probability of damage vs. fluence is calculated using a histogram of the fraction of resulting damaged sites vs. total number of test sites. The details of these obtained curves are presented in [33]. As we will show in this paper, the morphology for ps pulse laser induced-damage is more informative than for ns damage: the damage sites remain small, allowing for better inference of density, location, and sizes of initial laser-induced damage precursors. For pulses 1.8 ps and shorter, we will show that damage sites are smooth ablation pits a few hundred nanometers in depth. Roughness observed within the crater is typically due to material redeposited after vaporization (although small, high-density pits are still visible near the edges of the pits). Roughness and pitting become dominant for pulse lengths longer than 10 ps. Surface morphology is probed with confocal and atomic-force microscopy (AFM). We also provide high resolution scanning-electron microscopy (SEM) [19]. The 3D profiling capabilities of the former methods complement the high lateral resolution of SEM. The combination of methods is necessary to show whether a feature is due to local removal of material or due to debris from elsewhere. These factors help distinguish whether the non-uniform damage sites are due to non-uniform damage properties or due to inhomogeneous re-deposition processes.

2. Experimental Section

Corning 7980 fused silica, 2-inch round and 1-cm thick samples, were obtained from CVI-Melles Griot (Rochester, NY). Each optic was prepared using an optimized cleaning + etching process described as AMP3 at LLNL [34,35]. This process consistently yields high damage resistant optics. Several of these samples were coated with a silica coating tuned for ½-wave at 1053 nm and 0° (362 nm thick) using e-beam and plasma-ion assisted deposition (PIAD) at the Laboratory for Laser Energetics (LLE).

Laser-induced damage testing was performed at normal incidence using an in-air damage test station developed at LLNL. This test station is of similar design to the in-vacuum laser damage test station described in [36,37]. Without the physical constraints of the vacuum chamber, this station provides adjustable focal spot size on the sample and additional diagnostics. Laser damage is generated from an Optical Parametric Chirped Pulse Amplification (OPCPA) laser system similar to that described in [38,39]. It delivers 1053 nm pulses with energy up to 6mJ, at 10 Hz repetition rate. The pulse duration is tunable from ~0.4 ps up to 60 ps by changing the compressor slant distance. Pulse durations below 3 ps are measured with a single-shot frequency optical gating (FROG) device [40], while longer pulses are measured using a scanning cross correlator with a transform limited reference pulse. For this work the laser pulses are focused onto the sample, located in an air environment, with a f = 500 mm lens to initiate damage. The energy on target is computer-controlled with a motorized half waveplate located before two thin film polarizers.

Due to the inherent shot-to-shot fluctuations of the OPCPA laser, the laser energy, beam pointing and beam size need to be captured on every shot at 10 Hz. A fraction (5%) of the energy is directed to a reference beam path to diagnose the beam pointing and focal spot in a plane equivalent to the sample. The equivalent sample plane beam profile and laser energy are captured on every shot at 10 Hz in order to accurately determine the fluence delivered to the target. We developed a sophisticated data acquisition and controls system using LabVIEW (National Instruments PCIe-6351) to handle the beam diagnostics along with other tasks that need to be performed during damage tests, i.e. the number of shots delivered to the sample (via mechanical shutter), energy control via wave plate, in-situ damage detection and sample navigation.

We employ an automated 1-on-1 damage test methodology for an array of 300-400 pristine locations on a 0.5-mm grid following ISO 21254 [41]. An initial site is exposed to a starting fluence below the onset of damage for observable laser-induced modifications, and each subsequent line of sites is also exposed to a single pulse, but at progressively higher fluence. For analysis, we use the laser spatial beam profiles and energy calibrations at the equivalent sample plane to determine the peak laser fluence of each exposure and we classify each site as damaged or not damaged based on specified criteria described below. For the measurements in this paper, we use a 50 μm $1/e^2$ Gaussian beam to perform 1/1 damage tests. An *in situ* microscope based on a 10X, 0.28 NA long working distance Mitutoyo objective was used to acquire images of each site before and after laser damage testing. By subtracting the image before from the image after, we sensitively detected and classified laser-induced damage, as verified later using confocal microscopy. The fluence quoted for each shot is determined as the fluence at which 10% of the imaged beam fluence is higher than that fluence level. For each experiment in this study, we have computed the probability of damage as a function of fluence and reported the damage onset fluence corresponding to the 50% probability of damage. We use this metric to account for the variability of damage threshold over many (around 300-400) damage sites. As we will show, for short pulses, the difference is not large between 10% and 90% probability, but for pulses 30 ps and longer, there is a slow increase in damage as a function of fluence. The probability damage curves are discussed in [23].

Characterization and depth profiling of laser-induced damage sites is performed using laser scanning confocal microscopy (Keyence VK-100). We used a Nikon 100X 0.95

numerical aperture objective to produce high resolution images. The three dimensional information contained in the confocal microscopy is used to understand the morphology of the damage sites. This is supplemented by using AFM to determine the nanoscale morphology of the damage sites. For SEM, we used a Hitachi SU8000 Ultra High Resolution Field Emission SEM on samples coated with a 3-5 nm layer of gold-palladium.
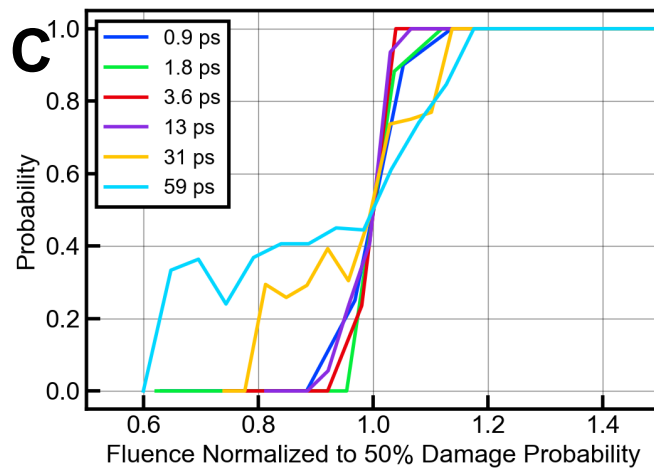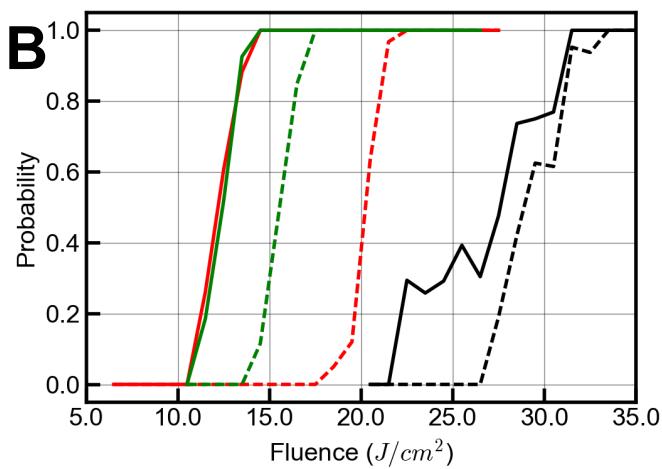
3. Results

3.1 Damage morphology classification and pulse scaling effects
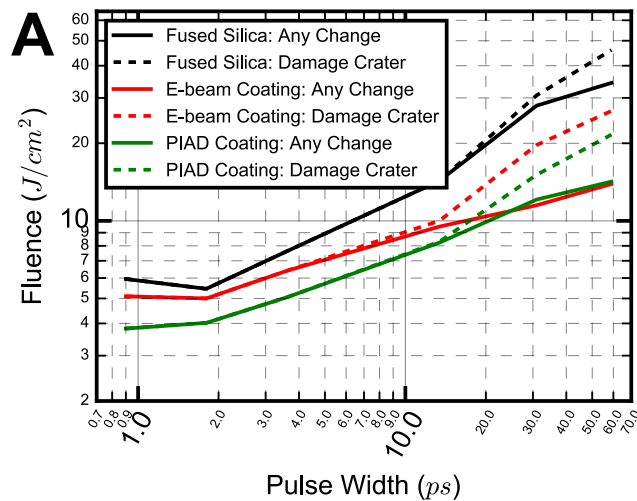
Fig. 1. A. Fluence damage onset (defined at 50% damage probability) for three samples: fused silica (black), e-beam silica coating (red), PIAD silica coating (green). For each sample there are two definitions of damage used. Solid lines indicate 50% probability of damage for any observed change, whereas for the dotted lines, only sites that include deeper damage pits with features at least 100 nm deep or that follow the spatial profile of the beam, i.e. near Gaussian. The deeper damage pits were initially observed as visible, dark pits using our *in situ* microscope. The size and depth of these pits were verified using confocal microscopy and AFM. B. 1-on-1 damage probability curves for 31 ps. Legend is same as in A. C. Probability of damage as function of fluence normalized by the fluence at which 50% of sites damage for pulse widths ranging from 0.9 to 59 ps.

Before discussing the morphology of the laser-induced damage sites and the implications for mechanisms, we first show the fluence for damage onset of fused silica and two silica coatings as a function of pulse widths between 0.9 ps and 59 ps. These results are a subset of the results on scaling from our companion paper [33] discussing the scaling laws and precursor densities for ps laser-induced damage. For the current results, we used the f = 500 mm lens which produces a 50 μm beam. The damage onsets shown in Fig. 1(a) correspond to the fluence at which 50% of the sites damaged. The main features of our results are that the damage onset occurs at consistently higher fluence for the fused silica than for the silica coatings. Additionally, the e-beam coating has a higher fluence for damage onset than the PIAD coatings. Similar to previous work [18,20], we see a flattening of the damage onset at lower pulse widths, and an increase in the damage onset with increasing pulse width. Fig. 1(b) shows example 1-on-1 damage probability curves as a function of fluence for 31 ps pulses from the same dataset in Fig. 1(a). Fig. 1(c) shows example 1-on-1 curves for all pulse widths tested here. As observed from Fig. 1(c), there is a sharp transition in the damage probability curve for 13 ps and shorter. Only a change of ~ 20% in fluence is required to go from 10% probability to 90% probability of damage. In contrast, at 31 and 59 ps, the shape of the damage curve widens and the probability of 10% to 90% damage requires a 100% increase in fluence.

We have performed photoluminescence lifetime imaging studies prior to performing laser damage experiments. We found that the two coated samples (e-beam and PIAD) had a much higher photoluminescence (PL) ~10X higher than the bare fused silica substrate (AMP3 cleaned). We have shown previously in [9] that a higher PL with broad emission and broad distribution of lifetimes [42] indicates a higher density of surface defects and typically leads to a lower damage onset, as observed here.

   Whereas other works, for example Stuart et al. [18,20], exposed each tested location to multiple laser pulses, here we use 1/1 damage tests that in order to distinguish between different mechanisms and sources of damage. We find that damage scaling with respect to pulse width is dependent on the definition of laser-induced damage, especially for the coating samples and at longer pulse widths greater than 10 ps. We have adopted a more inclusive and gradual definition of laser-induced modifications for both fused silica and silica coatings as follows. For damage occurring at lower fluence and pulse widths 10 ps and longer, we find regions of smooth, circular depressions with central pits (<100 nm depth) amidst pristine surfaces. This type of damage occurs both within and outside the peak fluence region of the laser beam, and does not necessarily grow with subsequent shots at the same fluence. In contrast, for all pulse widths at fluences above damage onset, we find a high density of damage pits within the peak fluence region that tend to grow more readily upon subsequent laser exposure. For pulse widths shorter than 10 ps, the difference in fluence required to obtain both classes of damage is very small as to be negligible; most often both classes of damage are visible for each site that damages. However, for pulse widths longer than 10 ps, the differences in fluence between the classes of damage increase. Hence, in Fig. 1 we have adopted two general classes of laser-induced modifications referred to as "Any change" and "Damage crater" (the former class includes the latter) to illustrate the general pulse scaling trends and enable quick comparison between the materials.

We now describe the damage morphologies in more detail. The detected damage used to generate the scaling law in Fig. 1 was classified into several distinct types. These damage morphologies are illustrated in Fig. 2. For bare fused silica substrate, we observed three main types of damage:

A) Standard material ablation crater ~50 μm wide (size of beam), 200 – 1000 nm deep. For pulse widths below 3 ps, the ablated surface is smooth whereas 3 ps and above, the surface roughness increases and gives way to high density pits.

B) High density of pits ~25-50 nm deep, ~50 nm wide, which occur at all pulse widths. At high enough fluence, these nanometer-sized pits can lead to localized damage.

C) Smooth, circular depressions 75-200 nm deep, 1-10 μm wide which are present both inside and outside the peak beam fluence.

For coated substrates, additional morphologies are in effect:

D) Crater > 300 nm due to removal of coating and material ablation.

E) Smooth, circular depressions with height and width similar to that found in type C).

Table 1 summarizes the surface roughness and profiles measured with a combination of confocal profilometry, AFM, and SEM. It is seen that the surface roughness increases with increasing pulse width, and that the high density pits and smooth circular depressions are shallow, 50-150 nm.
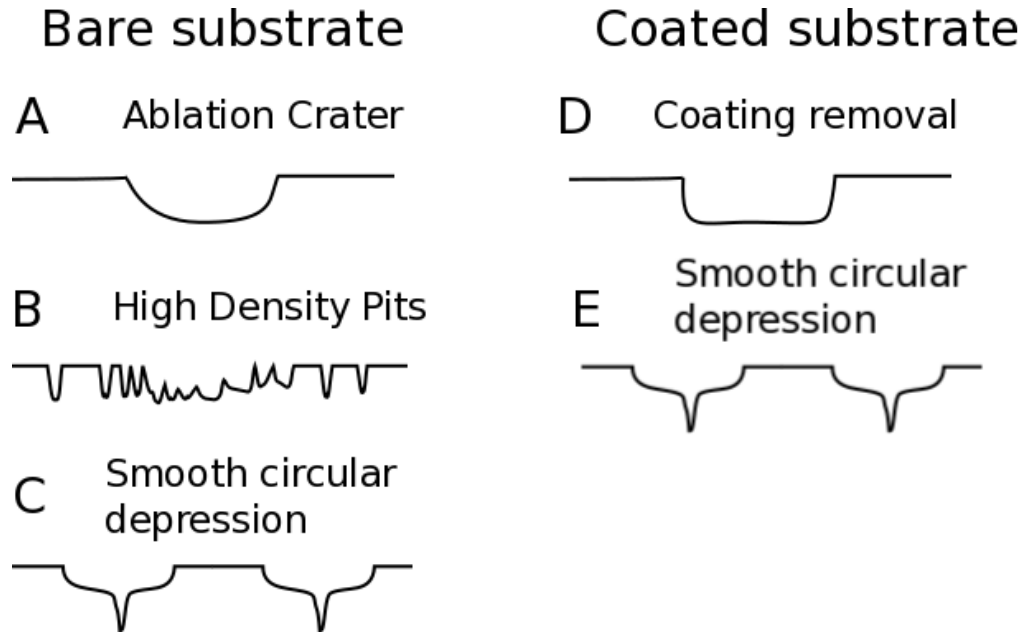

Fig. 2. Schematics of damage morphologies found in laser-induced damage for 1-60 ps pulse widths. For bare substrate: A. Smooth ablation crater of ~50 μm wide (size of beam), 200 – 1000 nm deep. B. High density pits ~25-50 nm deep, ~50 nm wide that coalesce to form large damage craters. C. Smooth, circular depressions 75-200 nm deep, 1-10 μm wide with small, deep pit associated with smooth, wide, shallow craters. For coated substrate: D. Crater from removal of coating and material ablation typically greater than 300 nm deep. E) Smooth, circular depression with small, deep pit in center, similar to those found in C).

Table 1. Surface roughness and profiles of damage morphologies observed from bare fused silica and coated substrates.

Pulse width	Surface roughness rms (nm)	Damage crater (nm)	High density pit depth (nm) at initiation	Smooth, circular depressions depth (nm)
Fused Silica				
0.9	30 ± 5	200-225	25	Not observed
1.8	40 ± 10	250-300	25	Not observed
3.6	100 ± 30	250-300	25	75-100
13	174 ± 80	250-400	50	100-150
31	220 ± 122	250-700	50	100-200
59	320 ± 138	250-1000	50	100-200
E-beam coated silica		(includes removal of coating ~362 nm)		
0.9	160 ± 20	400	Not observed	< 25
1.8	42.9 ± 9	400	Not observed	< 25
3.6	23 ± 7	400	Not observed	25
13	86 ± 24	300-600	Not observed	50
31	182 ± 23	300-700	Not observed	50
59	242± 50	400-750	Not observed	50
PIAD coated silica				
0.9	41 ± 4	400	Not observed	< 25
1.8	44 ± 4	400	Not observed	< 25
3.6	40 ± 7	350-400	Not observed	25
13	56 ± 12	350-600	Not observed	50
31	134 ± 10	400-650	Not observed	50
59	216 ± 40	400-650	Not observed	50

3.2 Fused Silica

The morphology of damage sites is an important indicator of the key laser-matter interaction processes involved. In order to illustrate the morphology of laser-induced damage, we display selected damage sites at fluences near the damage onset and well above onset. We first re-plot the damage scaling law for fused silica from Fig. 1 using data points that correspond to different fluence levels and thus the progression of different morphological features [Fig. 3]. We then show the images of the damage sites corresponding to those plots in Fig. 4. These images suggest that non-uniform damage and removal of material become much more significant, limiting cause of damage as pulse widths increase beyond 1.8 ps.

Fused silica samples prepared using the AMP3 process have a uniform, low-defect density surface [35] as measured using 351 nm, 3 ns laser-induced damage. The images in Fig. 4 show the morphological features we used to categorize damage sites and also show the non-uniform nature of laser-induced damage on fused silica surfaces. For 0.9 ps to 13 ps pulses, there is a sharp onset of laser-induced damage with increasing pulse energy. Damage generally occurred at the center of the Gaussian beam where the intensity is the highest. For pulse widths shorter than 3.6 ps, the morphology of the damage site well above damage onset is generally a smooth, shallow crater 200 nm deep, characteristic of fast ablation and vaporization as observed in the "high" column of Fig. 4 for <3.6 ps. Formation of these

smooth pits has been attributed to laser induced optical breakdown from avalanche ionization and multiphoton absorption [20,43,44]. However, near the edges of the sites, roughness is observed. Although some of this is due to re-deposited material, AFM and SEM imaging shown below reveal pits in the material that indicate inhomogeneities or isolated defects. Isolated defects clearly play a significant role at pulse widths of 13 ps or longer, but our results suggest that they may play a role even at shorter pulse widths. Smooth, circular depressions such as those seen in the "low fluence" image for 59 ps in Fig. 4 indicate that uniform material properties are not the only factor in laser induced damage of fused silica with ps pulses. Locations of these sites do not follow the peak of the laser beam as do the rough pits observed, and they clearly indicate variations in surface damage propensity, which have also been observed in [45,46].
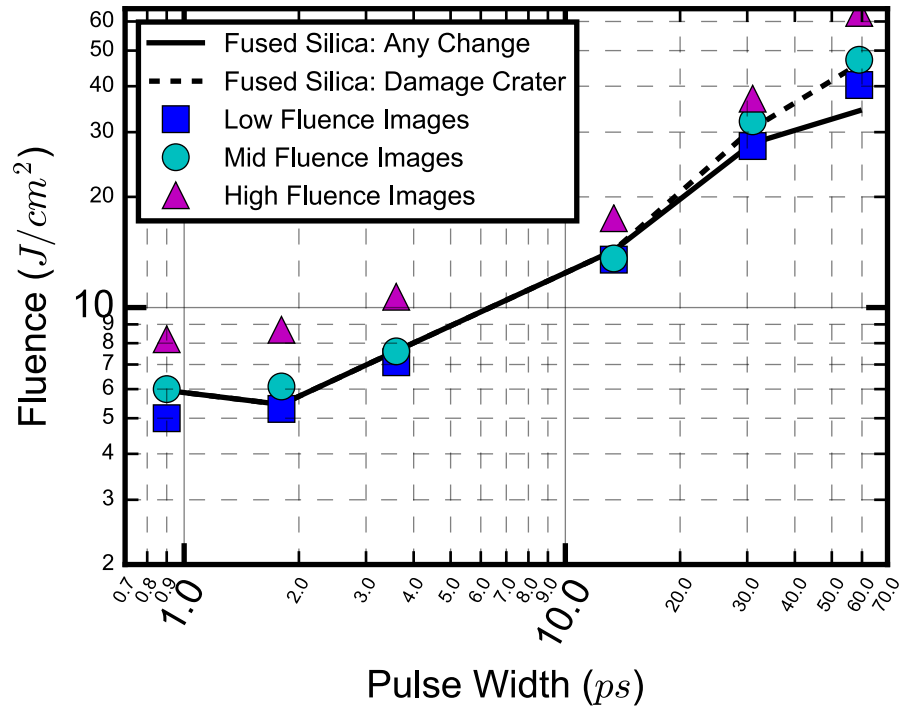

Fig. 3. Plot of fluences for images of damage sites in Fig. 4 overlaid on to the 50% damage probability for fused silica. Blue squares are for low fluence images, where damage just begins to occur (~10% damage level). Cyan circles are for mid-fluence images (~50% damage level). Magenta triangles are for high fluence images (~100% damage level).

For higher depth resolution, we use AFM to profile regions slightly above the damage onset that contains small nanoscale pits. AFM shows that these are not simply due to re-deposited material, but are in fact due to isolated regions which are more susceptible to damage. For 13 ps or longer, we do not observe smooth ablation craters, but rather very rough craters and smooth, circular depression sites [Fig. 5]. Figure 5 shows regions of images corresponding to those in Fig. 4. Figure 5(a) shows the small region for the damage site for a 13 ps pulse. In the AFM image, it is clear that there are regions of unaffected surface with small nanoscale pits formed interspersed with re-deposited material. The lineout in Fig. 5(d) shows pits between 20 and 40 nm deep. As the pulse length increases to 31 ps, these pits grow in depth and are now surrounded by a ring of redeposited material [Fig. 5(b)]. A high

resolution SEM image of the same region as Fig. 5(a) is shown in Fig. 5(g). Figure 5(h) depicts a magnified view of the site for which the line-out is taken in Fig. 5(b). The green lines in Figs. 5(g-h) depict approximately where the line-outs are taken in Figs. 5(a-b). Similar high-density pits are observed at high fluence for 59 ps.
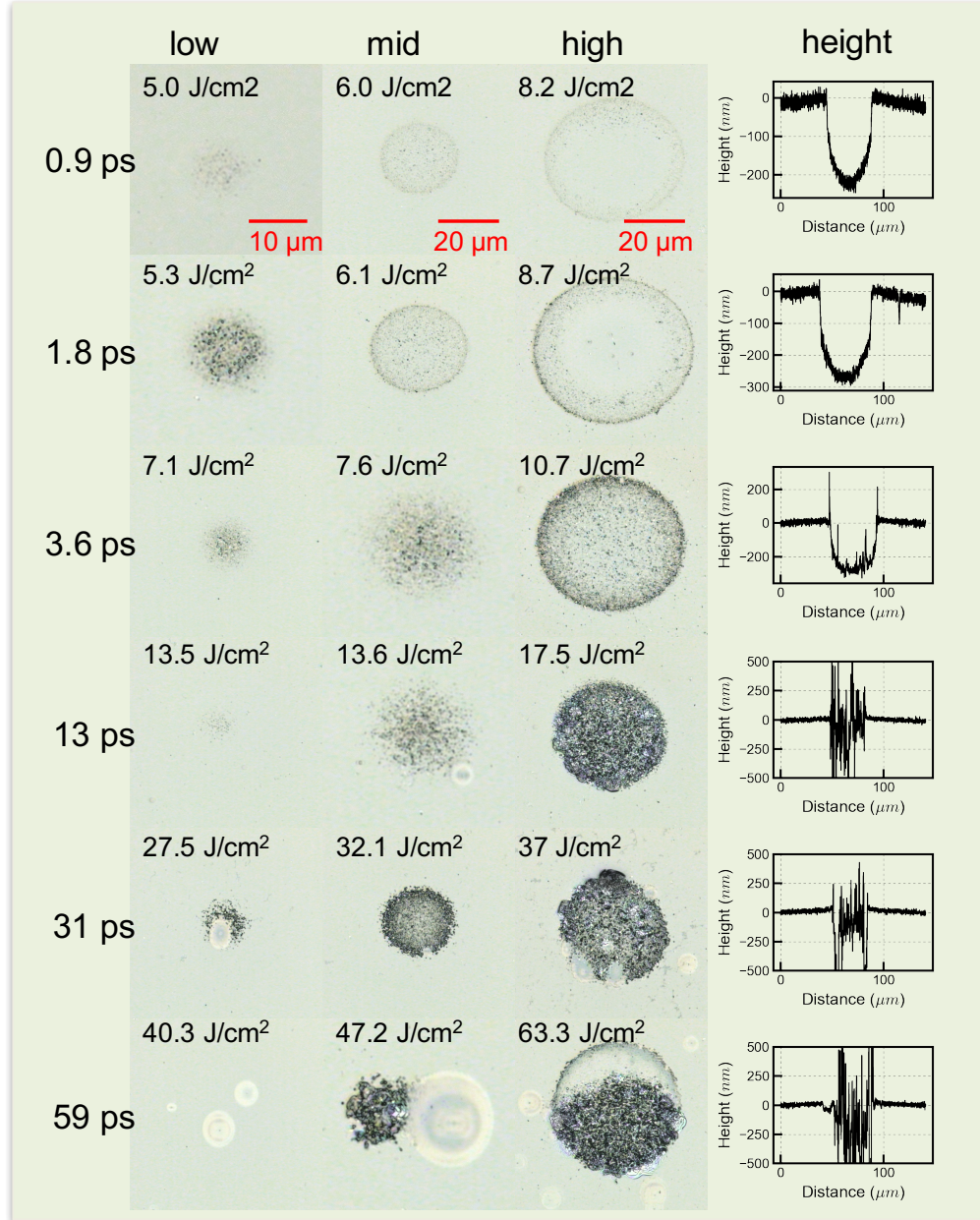

Fig. 4. Confocal images of laser induced damage sites as a function of pulse width and fluence for fused silica. The first three columns of images show the damage sites at low fluence, mid fluence, and high fluence for each pulse width. The last column shows the line-out profile corresponding to the high fluence column with 0 μm indicating the surface. Confocal images of damage sites near the damage onset (low) suggest that extrinsic factors affect the damage onset and mechanisms. Smooth, circular depression sites appear in the 13-59 ps range. For higher fluences, the smooth ablation craters at short pulses (0.9 ps to 1.8 ps) give way to extremely rough crater for longer pulses. The orange line across the image on the "high" column corresponds to the line-out in the last column. The orange arrow in the last column indicates the edge of the damage site.
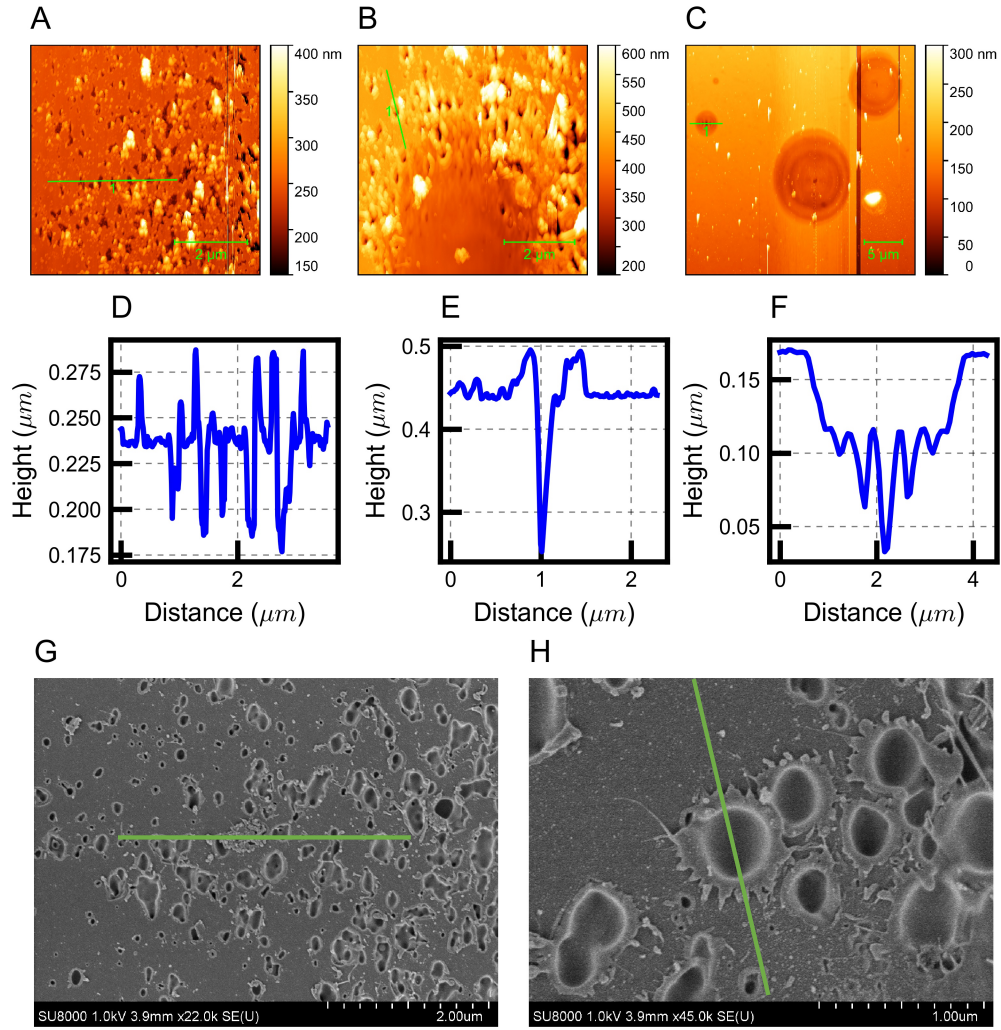
Fig. 5. A. AFM image of single shot damage site for 13 ps pulse near the onset of damage. Same site as image for 13 ps and 13.5 J/cm^2, "low" column in Fig. 4. B. AFM image of single shot damage site for 31 ps pulse width just above damage onset. Same site as image for 31 ps, "low" column" in Fig. 4. C. AFM image of single shot damage site for 59 ps pulse width near the onset of damage. Same site as image for 59 ps, 40.3 J/ cm^2 in Fig. 4. D-F. Lineouts from corresponding images. The surface of the substrate is located at 0.00 μm on the y-axis. The locations of the lineouts are marked in green. G) SEM image corresponding to the region in A with the line in green approximately same location as A. H) SEM image corresponding to magnified view in B with the line in green approximately same location as B.

For longer pulse widths (13, 31, and 59 ps), smooth, circular depression sites that do not correspond to the peak of the beam are also observed. For 31 ps, one of these sites is observed in Fig. 5(b) (same as Fig. 4, 31ps, 27.5 J/cm^2) as the smooth surface toward the bottom of the image. Similar isolated damage sites are also visible in the image in Fig. 5(c). These micron-scale sites are very smooth and are 50 to 200 nm deep. Some of these sites are located within the peak beam intensity and overlaid over the smaller pits, and others are located near the wing of the beam profile. These smooth, circular depressions show an interesting morphological structure in the lineout of Fig. 5(f). We suggest that these

structures are due to laser-assisted absorption fronts originating from isolated precursors, similar to what is seen for nano-second pulses [4,45,46]. The main differences are the shorter pulse widths, the longer wavelength (1053 nm vs. 351 nm) and the fact that these damage sites are on the entrance surface, which does not allow deep pits to form. The emergence of these larger, smooth, circular damage sites for pulse widths at 13 ps and longer shows that there are two distinct damage morphologies, suggesting two precursors types which occur with vastly different densities and characteristic fluences. We did not observe what could be called homogeneous ablation for these pulse widths. The isolated damage sites are included in the solid lines in Figs. 1 and 2, but are excluded in the "damage crater" curve of those figures.
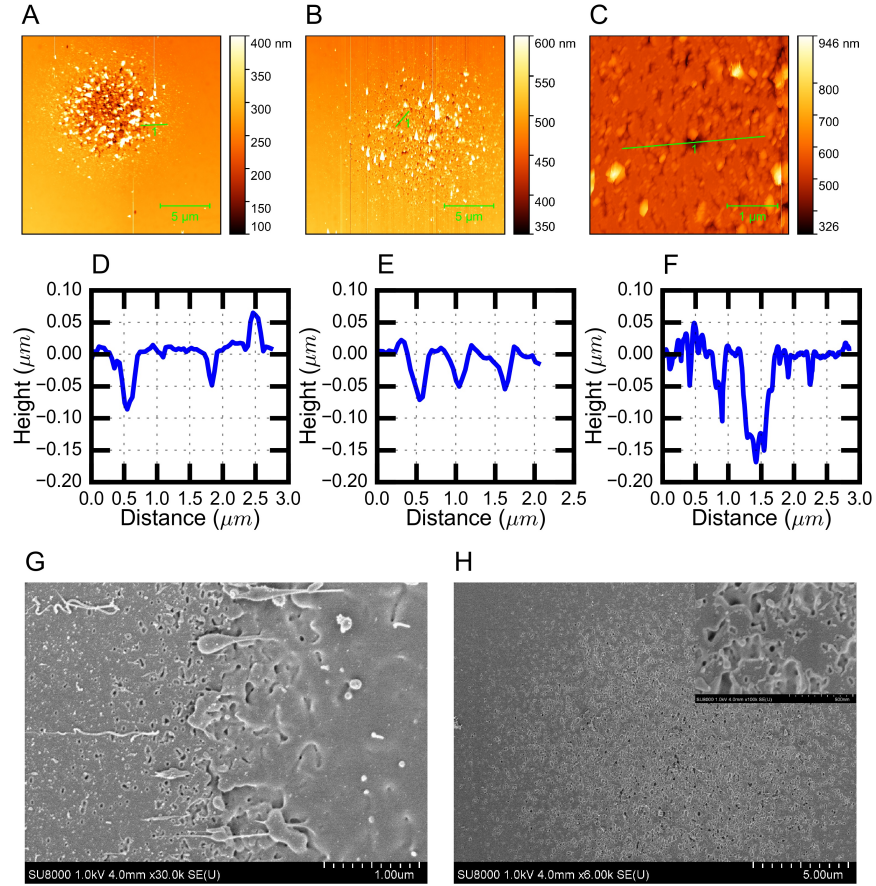

Fig. 6. A. AFM image of single shot damage site for 1.8 ps pulse just above damage onset. Same site as image for 1.8 ps, 5.3 J/ cm^2, "low" column in Fig. 4. B. AFM image of single shot damage site for 3.6 ps pulse width just below crater formation, but above damage onset. Same site as image for 3.6 ps, in Fig. 4. C. Zoom in on same site as in B in order to show structure of surface after laser shot. D-F. Lineouts from corresponding images above lineouts. . The surface of the substrate is located at 0.00 μm on the y-axis. The locations of the lineouts are marked in green. G. SEM image corresponding to an unspecified region on image A. On the left edge of the ablation pit that sits toward the right, many small pits observable. H. SEM image corresponding to the site in B. A region similar to that for the line-out in B is shown as an inset at higher magnification.

For shorter pulses between 0.9 s and 1.8 ps, it is not clear if isolated defects play a significant role in damage initiation [Fig. 6], although effects from isolated defects are visible. For the damage site formed with a 1.8 ps pulse [Fig. 6(a)] near the damage onset [5.3 J/ cm^2, "low" column in Fig. 4], the formation of a crater following the beam profile is readily

observed. Re-deposited material distributed around and inside the damage site is also obvious as observed from the peak in lineout in Fig. 6(d). However, even with this pulse width, there is evidence of small pits forming in the lower fluence regions outside the main damage site from the lineout. This is particularly evident in the SEM image from Fig. 6(g) for another damage site with 1.8 ps pulse width. In this case, on the left edge of the ablation pit that sits toward the right, there are many small pits observable. For the slightly longer pulse width of 3.6 ps near the damage onset ("low" column, 7.1 J/ cm^2), the smooth ablation crater following the beam profile disappears, replaced by a rough crater with a distribution of small pits and re-deposited material [Fig. 6(b)]. Pit depths of 60 to 100 nm are typical [Fig. 6(e)]. Zooming in to observe smaller features [Fig. 6(c)], it is possible to see that just as at longer pulse widths, there is an untouched surface interspersed with small pits and re-deposited material. The size of the high density pits tends to increase with pulse duration, and the density tends to decrease.

3.3 Deposited silica coatings

E-beam coatings are the most commonly used coatings for multilayered dielectric coatings. We study the morphology of the e-beam coatings using the same methods and similar figures as for fused silica in the previous section. In addition to the laser induced damage onset being lower for the coatings compared to fused silica [Figs. 1, 7], the morphology has significant differences for these coatings. For short pulses, especially those 3.6 ps or shorter, most often complete coating removal occurs upon laser exposure [Figs. 8 and 9]. In contrast, for longer pulses, there are much smaller individual pits and depressions that form at lower fluence. As detailed later, these depressions have a morphology more similar to the smooth, circular depressions observed on fused silica more than the high-density pits. At higher fluence, the individual depressions combine to form a larger, rough crater. The smaller individual depressions that form at low fluence and longer pulses are also visible at short pulses as small gray circles [see Fig. 8: 59 ps, 13.4 J/cm^2], but are much less prominent. It is not clear if the emerging isolated depressions indicate that defects play a role in limiting laser damage performance or if there is only bulk material ablation limiting performance. However, based on these images, isolated precursors do play a major role in laser-induced damage for 3.6 ps and longer in these coatings.
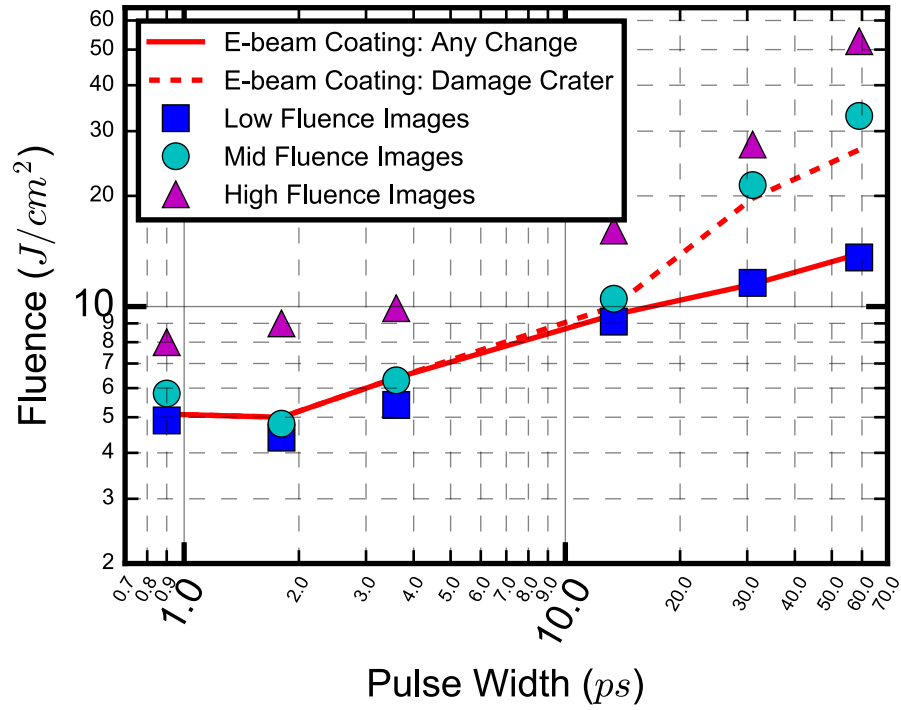
Fig. 7. Plot of fluences for images of damage sites overlaid on to the 50% damage probability for e-beam coating of silica. Blue squares are for low fluences images (any change observed). Cyan circles are for mid-fluence images (~50% damage probability). Magenta triangles are for high fluence images (100% damage).

If we categorize the circular depressions observed at low fluence as damage, then we obtain the solid red line in Figs. 1 and 7. On the other hand, if we exclude the circular depressions unless they appear dark in the *in situ* camera, we obtain the dotted red line in those same figures. As with the fused silica sample, we verify the depth of these small pits using confocal microscopy and AFM.
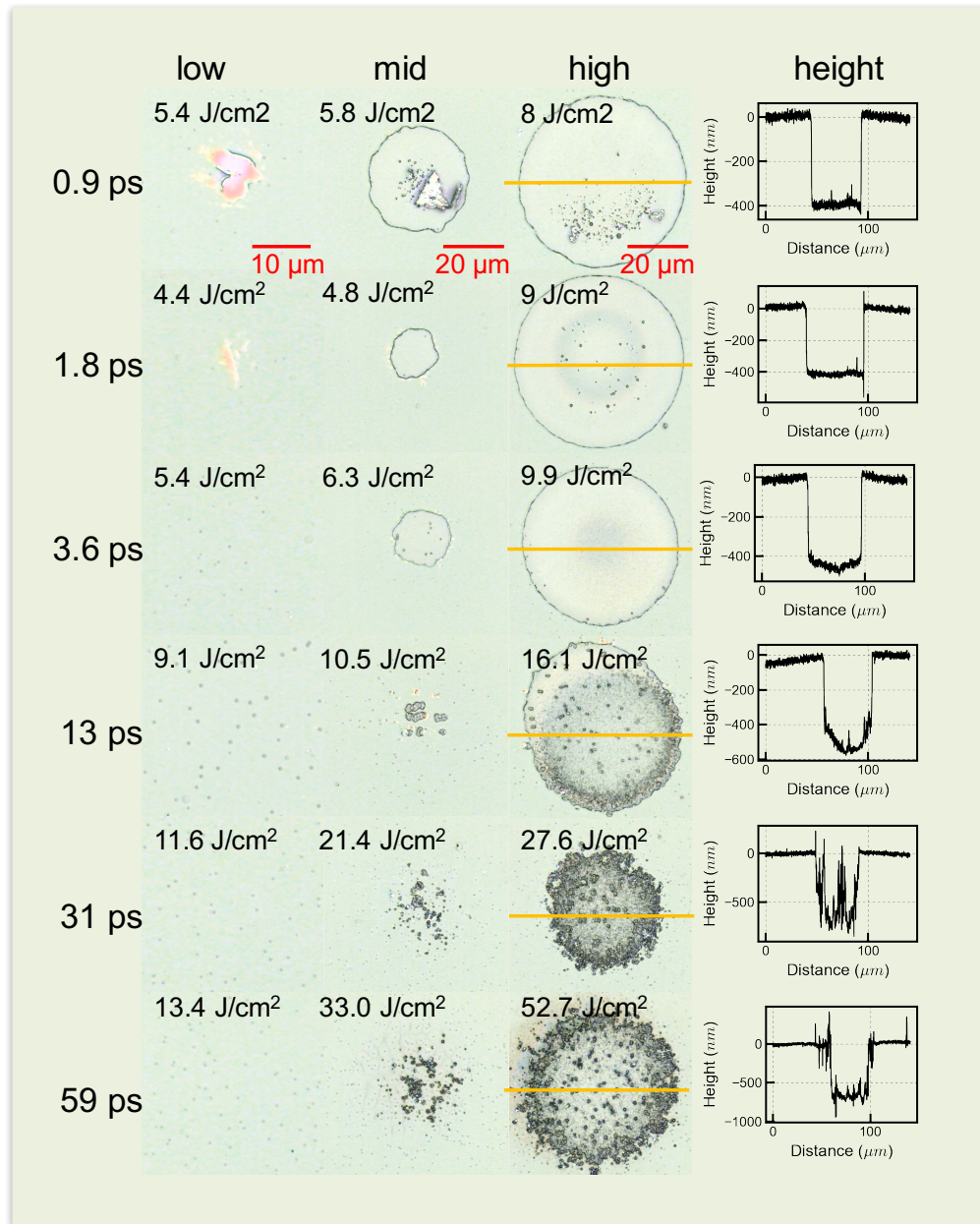
Fig. 8. Confocal images of laser induced damage sites as a function of pulse width and fluence for an e-beam silica coating. The first three columns of images show the damage sites at low fluence, mid fluence, and high fluence for each pulse width. The last column shows the line-out profile corresponding to the high fluence column with 0 μm indicating the surface. Confocal images of damage sites near or just below damage onset (low fluence column) show evidence of isolated precursors for laser-induced damage. The isolated precursors appear as small gray circles in the confocal images. The isolated damage sites appear significantly more prominent in the 13-59 ps range. For short pulses 0.9 ps, 1.8 ps and 3.6 ps, complete coating removal is the most common morphology observed. In contrast, damage sites for pulse widths of 13 ps and greater exhibit rougher damage sites that appear to be conglomerations of many small damage sites. The orange line across the image on the "high" column corresponds to the line-out in the last column.

The confocal images shown in Fig. 8 show the basic features of laser-induced damage for a single silica layer formed using e-beam deposition. The first column shows primarily the circular depressions formed at low fluence observed as the small gray circles. These are more prominent at longer pulse widths, but are also visible at 0.9-3.6 ps. The shot resulting in the damage site in the upper left hand corner for 0.9 ps is very near the damage onset (0.9 ps, 5.4 J/cm^2). The coating is peeled up but not removed and the circular depressions and high density pits are visible. For higher fluences, the coating is removed, and debris is left behind within the pit for these short pulse widths. It is not clear if the circular depressions are important to the coating removal, or incidental. A lineout profile corresponding to the high fluence damage sites is on the last column of Fig. 8. It can be seen from the line-out that the coating is completely removed from the substrate. Since the coating is nominally 362 nm thick, and given this is a single shot experiment, there is no evidence from the confocal images that mass removal from the bulk substrate has occurred below 3.6 ps. The height profile for 0.9 and 1.8 ps in Fig. 8 shows ~400 nm rather than 362 nm. We believe this discrepancy is not due to measurement error, but rather bowing around the edges. One possible reason is during the laser-film interaction shock and heat may cause a local expansion of the film.

However, as pulse width increases, the depth increases beyond the thickness of the coating. The circular depressions that show up at low fluence play a more obvious role at longer pulse widths of 13 ps or longer [Fig. 8]. For example in Fig. 8 at 31 ps, it can be seen that, when transitioning between low (11.6 J/cm^2) to mid (21.4 J/cm^2) to high (27.6 J/cm^2) fluence, these circular depressions coalesce to form large pits in the coating. The transition between the barely visible pits in the leftmost column and the deeper, more obvious pits in the rightmost column corresponds to the 50% damage probability in Fig. 7 indicated by the solid red line.

The AFM images in Fig. 9 reveal the nanoscale features of the damage sites for e-beam coatings. In Fig. 9(a), a bulge in the coating is visible as well as the circular depressions. A lineout of a circular depression show depths of 60 to 80 nm [Fig. 9(d)]. This line-out region can be observed in finer detail on the SEM image in Fig. 9(g). The bulge in the coating appears to be caused by something other than the circular depressions at the surface: perhaps something deeper in the coating or even at the coating-substrate interface. It may be that defects similar to those seen at the surface occur deeper in the coating, and lead the coating to detach. This image does not suggest a homogeneous ablation process of the surface. However, for higher fluences, the coating is cleanly removed leaving behind a circular hole as seen in Fig. 8. Regardless of whether homogeneous processes or isolated defects dominate the damage process, it is clear that isolated defects do affect local regions. For longer pulse widths, the circular depressions lead to deeper pits. For 13 ps, the pits are 80-120 nm deep as seen in Figs. 9(b) and 9(e), and even deeper for 31 ps in Figs. 9(c) and 9(f). In Fig. 9(c) and 9(g), some of the isolated pits have a surrounding ringing 10 to 20 nm deep similar to those seen for smooth, circular depressions on fused silica surfaces from the previous section. Other small pits do not have this ring, possibly indicating two classes of precursors. The differences between the deeper pits without the ring and the shallower pits with the ring can be seen by comparing the SEM image in Fig. 9(h) to the AFM images in Figs. 9(c) and 9(f). The deeper pits appear to affect the surrounding coating less, whereas the shallower pits affect the surrounding coating more. These images suggest that the sites without the ring are from precursors within the coating rather than at the surface of the coating. For the e-beam coating at pulse widths from 1-60 ps, the damage morphology is dominated by isolated precursors or inhomogeneous properties over the surfaces and within the coating material.

Finally, we also studied the morphology of the PIAD silica coating. The PIAD silica coating behaves similarly to the e-beam coating in terms of laser induced damage morphology (not shown). The laser damage onset is lower than for the e-beam coating [Fig.

1], and the small pits are more visible at lower beam fluences for short pulses including 0.9 ps and 1.8 ps.
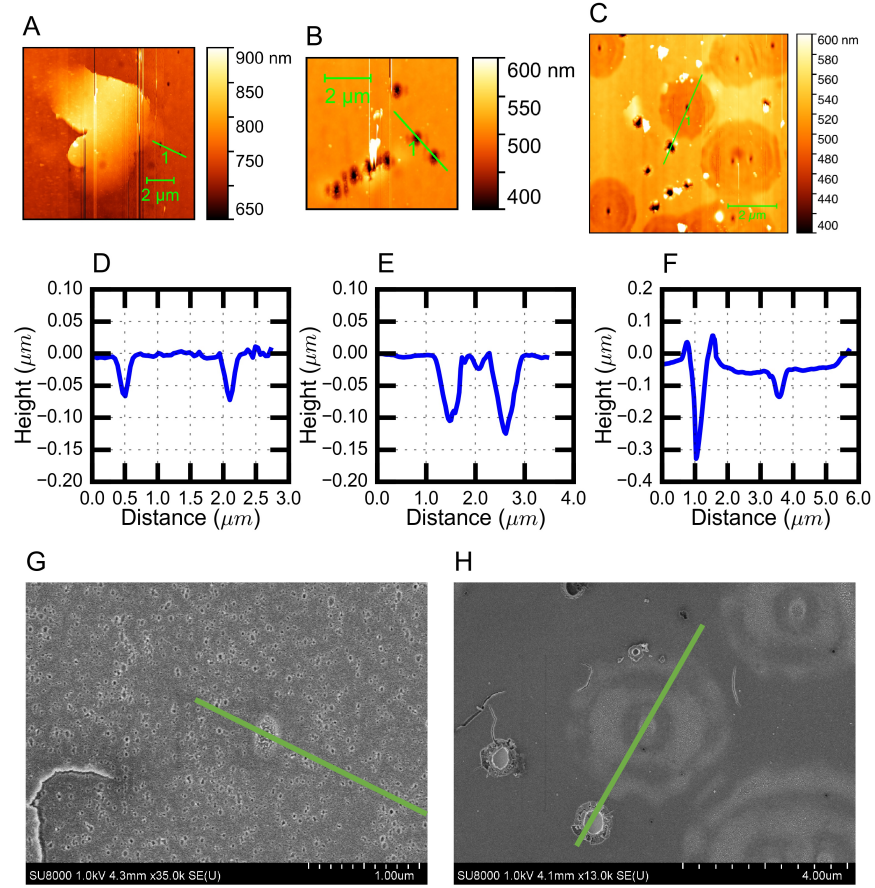

Fig. 9. A. AFM image of single shot damage site for 0.9 ps pulse near the damage onset. Same site as image for 0.9 ps, top row in Fig. 8 ("low" column, 5.4 J/cm^2). B. AFM image of single shot damage site for 13 ps pulse width near the damage onset ("low" column, 9.1 J/cm^2). C. AFM image of single shot damage site for 31 ps pulse width near the onset of damage [dashed line in Fig. 7]. D-F. Lineouts from corresponding images above. The locations of the lineouts are marked in green. G. SEM image corresponding to region of line-out in A showing small, isolated damage site visible in confocal microscopy as well as numerous, nanoscale pits in the coating. H. SEM image of C, showing SEM images of pits corresponding to line-out in F.

4. Discussion

Three different morphologies were observed for 1-60 ps damage with 1053 nm pulses. Smooth ablation craters, high-density pits, and smooth, circular depressions with a central pit are all observed. These morphologies indicate alternative damage mechanisms that should be taken into account in modeling efforts. A homogeneous damage process would create a smooth crater with roughness only created by re-deposition of ablated material. For pulses 1.8 ps and shorter, we do see regions with smooth ablation craters. However, for all other cases, the morphology of the damage sites indicates a local defect or region with higher susceptibility to damage. The morphologies observed at pulse widths 3 ps and longer of small, high-density pits and smooth, circular depressions of varying size and density point to a shift in mechanisms for these pulse widths. High-density submicron pits have been observed previously for SiO$_2$ and HfO$_2$ [2,47,48]and in fused silica for pulse widths from 50

fs to 2 ps pulses [49]. We extend observation of these pits up to 59 ps, where the sizes of the high-density pits increases with pulse width, while the density observed decreases.

Changing the definition of damage based on particular morphological features affects the scaling laws observed for laser-induced damage. Hence, caution is needed in applying existing models that are solely based on multiphoton ionization and avalanche ionization to the damage processes for ps pulses, especially for 10 ps and longer. This shift in mechanisms near 10 ps was postulated in [20], although the single-shot studies here provide additional insight into the nature and distribution of defects responsible for the defect-dominated mechanism for longer pulse widths. It is important to note that nearly all the damage observed occurs at the surface. For the short pulses, the fundamental material ablation is limited to shallow craters due to plasma shielding. However, for pulses 3 ps and longer, we see small pits and depressions primarily at the surface. The only possible exceptions are the complete removal of the coating for shorter pulses and the observed deeper pits as noted in Fig. 9(h). There is clearly a larger propensity for laser-induced damage precursors to be on the surfaces of fused silica and silica coatings.

One issue not yet addressed is whether the inhomogeneities observed are due to high spatial modulation effects on the beam due to non-linear effects, especially since these experiments were performed in air. There are several arguments against this. First, separate experiments were performed in vacuum with a larger beam, and the same morphological features and damage probabilities were observed for fused silica and the silica coatings. Second, the densities of the pits observed varied considerably between the e-beam coating and fused silica under similar conditions. Very high densities of small pits were observed with the e-beam coating with 0.9 ps pulse [3×10^9 cm^{-2} in Fig. 9(g)], vs. (3×10^8 cm^{-2}) for fused silica. If the beam were responsible for the distribution of pits, we would not expect this variation between samples. Third, the smooth, circular depressions, for example in Fig. 5, do not have any roughness observed, indicating that it is possible to have very smooth material removal with the laser beams used. Finally, the roughness observed increases with increasing pulse width (Table I). This is contrary to what would be expected for non-linear effects; we would expect much fewer non-linear effects on the beam due to the lower intensity at longer pulse widths.

In the Results section, we suggested that the smooth, circular depression damage sites were due to laser-assisted absorption fronts originating from isolated precursors, similar to what is seen for nano-second pulses [11]. In that work, absorption fronts that moved with an intensity-dependent velocity were observed.   The velocities scaled with intensity approximately with the power $I^{0.8}$, near a ratio or velocity to intensity of 0.3 (µm/ns) / (GW/cm^2). It was suggested that the velocity scaling would be valid for higher intensities, but the large fractures associated with rear-surface ns laser-induced damage prevented verification. Using the power law of $I^{0.8}$, we expect a ratio of about 0.1 (µm/ns) / (GW/cm^2) at our intensities. We use two examples of the smooth, circular depressions observed for fused silica in Fig. 4 to compare with the ratio from [11]. For the mid-range damage site for 13 ps pulses in Fig. 4, the circular depression at the lower right occurs in a region with a fluence of approximately 11 J/cm^2 (determined using beam profile). It's radius was 2.5 µm, leading to a ratio of 0.2 (µm/ns) / (GW/cm^2). For the low-range damage site for 31 ps pulses in Fig. 4, the circular depression in the center occurs in a fluence region near the peak fluence of 27.5 J/cm^2.   The radius of 3 µm corresponds to a ratio of 0.1 (µm/ns) / (GW/cm^2). Similarly, the circular depression for the e-beam coating damage with a 31 ps pulse in Fig. 9(c) and 9(f) occurs at about 20 J/cm^2. It's radius is 2 µm, corresponding to a ratio of 0.1 (µm/ns) / (GW/cm^2). Given the much higher intensities, the longer wavelength, and the different orientation of the laser (front surface damage vs. rear surface), the agreement

between the ns and ps results is impressive, suggesting that laser-assisted absorption fronts cause the smooth, circular depression damage sites in the ps regime.

5. Conclusion

For pulse widths between 1 and 60 ps, non-homogeneous properties and isolated precursors play a role in laser-induced damage in both fused silica and silica coatings. The morphology of the resulting damage strongly indicates localized precursors to damage, strongly indicating that damage with 1-60 ps pulses cannot be explained solely by using a multiphoton/avalanche ionization model applied to a homogeneous material. The damage process appears closer to an intrinsic process at 1.8 ps and below, although there is considerable evidence that defects or surface inhomogeneity play a role near damage onset. The effects of isolated defects play a more important role in the silica coating samples as illustrated most clearly in Fig. 9, which are of the most practical importance for laser systems in this pulse width range due to the use of reflective multi-layer optics rather than transmissive optics. In order to model the damage processes correctly, it will be necessary to account for the varying physical processes that contribute to laser-induced damage with ps pulses. The results here suggest that it will be important to understand the nature of these isolated defects and the effects of inhomogeneous surface properties on the laser-induced damage processes in achieving optics with enhanced resistance to laser-induced damage.